Mechanical behavior of steel tube encased high-strength concrete composite walls under constant axial load and cyclically increasing lateral load: Experimental investigation and modeling

Liang Bai[*1], Huilin Wei[1], Bin Wang[1], Fangfang Liao[1], Tianhua Zhou[1] and Xingwen Liang[2]

[1]*School of Civil Engineering, Chang'an University, Xi'an, Shaanxi, 710061, China*
[2]*School of Civil Engineering, Xi'an University of Architecture and Technology, Xi'an, Shaanxi, 710055, China*

Abstract. This paper presented an investigation into steel tubes encased high-strength concrete (STHC) composite walls, wherein steel tubes were embedded at the boundary elements of high-strength concrete walls. A series of cyclic loading tests was conducted to evaluate the failure pattern, hysteresis characteristics, load-bearing capacity, deformability, and strain distribution of STHC composite walls. The test results demonstrated that the bearing capacity and ductility of the STHC composite walls improved with the embedding of steel tubes at the boundary elements. An analytical method was then established to predict the flexural bearing capacity of the STHC composite walls, and the calculated results agreed well with the experimental values, with errors of less than 10%. Finally, a finite element modeling (FEM) was developed via the OpenSees program to analyze the mechanical performance of the STHC composite wall. The FEM was validated through test results; additionally, the influences of the axial load ratio, steel tube strength, and shear-span ratio on the mechanical properties of STHC composite walls were comprehensively investigated.

Keywords: composite walls; FEM analysis; high-strength concrete; mechanical behavior; steel tube

1. Introduction

Reinforced concrete walls are extensively employed as primary lateral resistance systems in high-rise buildings owing to the large load-bearing capacities and stiffness values. The high strength concrete (HSC) has many advantages including high strength, excellent durability, and high impermeability. Therefore, the HSC has been widely applied to the lower stories of high-rise buildings such as beams, columns, walls, and other load-bearing components. The construction of HSC walls can reduce the section size, effectively lightening the weight of the component, and eliminate seismic action. Generally, the toughness and ratio of the tensile strength to the compressive strength decrease with increasing compressive strength of concrete. The ductility of HSC walls is lower than that of common concrete walls owing to the brittleness of HSC, which limits its applicability in seismic zones (Paulay and Priestley 1992, Teng and Chandra 2016, Li *et al.* 2020, Younas *et al.* 2021).

A variety of steel profiles and tubes have been combined with common concrete walls to form steel and concrete composite walls, which have been increasingly employed in essential lateral-force resistance components (Tong *et al.* 2005, Curkovic *et al.* 2019, Gao *et al.* 2018). Concrete filled steel tubes are characterized by a high strength, stiffness, and good deformability owing to the presence of a

triaxially confined core (Liang *et al.* 2018, Huang *et al.* 2012). Therefore, to improve the mechanical performance and seismic behavior of common concrete walls, several studies have proposed the use of steel tube reinforced concrete (STRC) composite walls, which are formed by embedding steel tubes at the boundary elements of common concrete walls (Ji *et al.* 2015, Xu *et al.* 2017, Liao *et al.* 2009, Qin *et al.* 2020). Such composite walls have been demonstrated to exhibit excellent cyclic behavior with increased strength, high ductility, and good energy dissipation capacity. For instance, Qian *et al.* (2008, 2010) conducted experimental studies on the seismic behavior of STRC composite walls under a high axial force, and the results revealed that the deformation capacity of such composite walls improved. Cao *et al.* (2008a, 2008b, 2008c) and Zhao *et al.* (2020) studied the cyclic performance of composite walls with concrete filled steel tube columns, and the results indicated that such types of composite walls exhibited good hysteretic performance. Fang *et al.* (2013) and Hou *et al.* (2019) analyzed the effects of the shear-span ratio, axial force ratio, and section type on the mechanical behavior of STRC composite walls. Bai *et al.* (2019) and Zhou *et al.* (2018) tested STRC walls with low shear-span ratios to investigate the influence of various parameters such as the number of steel tubes, vertical re-bars ratio, and concrete strength. Notably, the compressive strength of concrete adopted in existing studies is almost lower than that for C50.

Based on the abovementioned studies, it is evident that limited research has been conducted on the mechanical behavior of steel tube encased high-strength concrete

---

*Corresponding author, Ph.D. Professor
 E-mail: bailiang@chd.edu.cn

(a) Elevation of specimen STHSW2   (b) Section A-A of specimen STHSW2

(c) cross-section of HSCW1

(d) cross-section of STHSW2 and STHSW3

(e) Boundary element of specimens
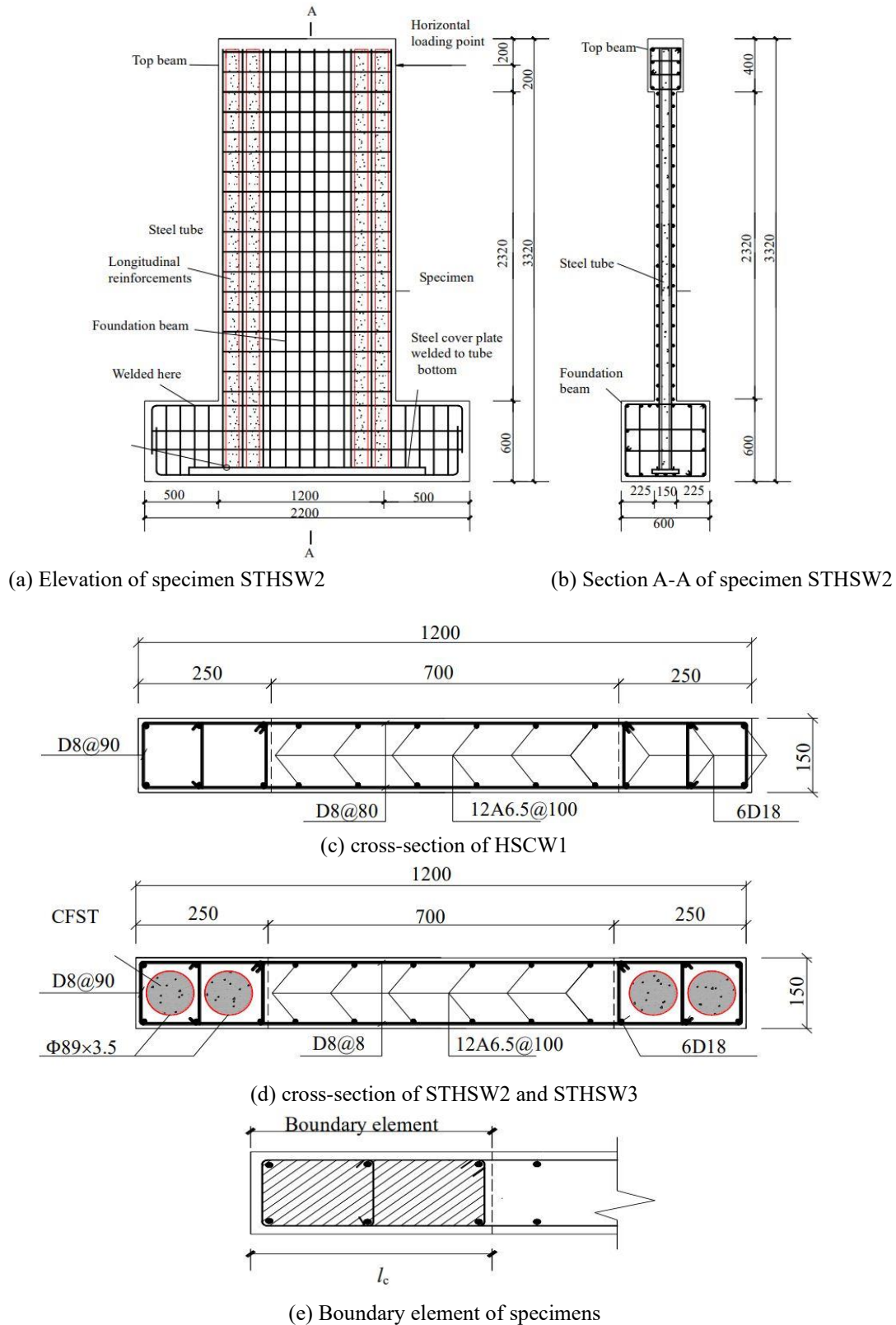
Fig. 1 Dimensions and construction details of specimens (unit: mm)

(STHC) composite walls; additionally, it is crucial to predict the load-carrying capacity of steel–concrete composite walls. Yang *et al*. (2014) analyzed the flexural bearing capacity of STRC composite walls without considering the confinement effect of steel tubes, and they

discovered that the adopted calculation method underestimated the flexural capacity of STRC composite walls, and the results were conservative. Zhang *et al*. (2021) evaluated the load-bearing capacity and ductility of HSC walls with boundary concrete-filled square steel tubes, and

Table 1 Material properties of steels

Steels	Yield stress/MPa	Ultimate strength/MPa	Elastic modulus /MPa
Tube Φ89 × 3.5	388.00	500.20	2.06×10^5
Rebar A6.5	390.69	522.08	2×10^5
Rebar D8	508.98	656.53	2×10^5
Rebar D18	476.30	648.90	2×10^5
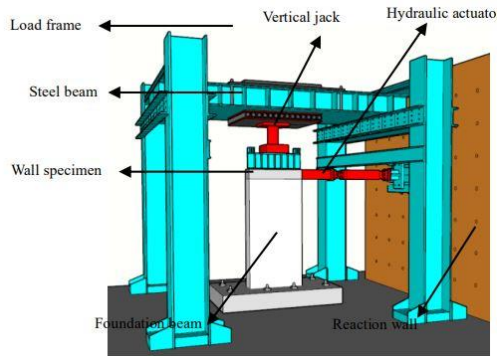
Fig. 2 Test setup
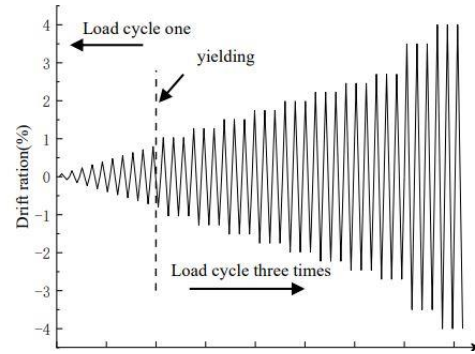
Fig. 3 Loading history

the results revealed that the square steel tube contributed towards improving the ductility; however, it exhibited limited improvement in the bearing capacity. Dang *et al*. (2022) investigated the cyclic behavior of precast steel–concrete tube composite walls, and an analytical method to predict the load-bearing capacity was established; however, the nominal compressive strength of the concrete employed in the study was 35 MPa.

To address the aforementioned research gaps, herein, STHC composite walls are proposed, wherein circular steel tubes are embedded at the boundary elements of the wall panels. Experiments are conducted on STHC composite walls and ordinary HSC walls. The failure modes, hysteresis characteristics, bearing capacity, ductility, and strain distribution of the specimens under cyclic loading are investigated. In addition, an analytical method is adopted to evaluate the flexural bearing capacity of the STHC composite walls, and the method is demonstrated to accurately predict the load-bearing capacity. A finite element modeling (FEM) is established and verified based on the test results. Further, a parametric analysis is adopted to investigate the primary factors affecting the mechanical properties of STHC composite walls.

2. Experimental program

2.1 Design of specimens

Three specimens were designed, tested, and labeled as HSCW1, STHSCW2, and STHSW3. Specimen HSCW1 was a common HSC wall, and the other ones were STHC composite walls. The specimens were designed to have strong shear and weak bending. According to this criterion, the distributed reinforcements ratio, axial load ratio, strength and cross-sectional areas of the steel tubes, and concrete strength of STHC composite walls were

determined.

As shown in Fig. 1, the dimensions of each wall were as follows: 1200 mm × 150 mm. The walls were 2320 mm high, and the shear-span ratio per wall was 2.1. In contrast to specimen HSCW1, specimens STHSW2 and STHSW3 were reinforced using Φ89×3.5 steel tubes at the walls' boundary elements. The stirrup configurations were D8@90 for all specimens. The vertical and horizontal distribution reinforcements for the webs of wall panels were A6.5@100 and D8@80, respectively. The longitudinal reinforcements used for the boundary elements were six D18 reinforcements for specimen HSCW1 and six A6.5 reinforcements for specimens STHSW2 and STHSW3. The amount of transverse reinforcements at the boundary elements was expressed by the stirrup characteristic value λ_v, specified in GB50010 (2010) ($\lambda_v = \rho_v f_{yv}/f_c$, where ρ_v denotes the stirrup ratio, and f_{yv} and f_c denote the yield strength of the transverse reinforcement and the axial compressive strength of concrete, respectively). According to GB50010 (2010), the stirrup characteristic value λ_v should be at least 0.2, and the depth of the boundary elements l_c was not less than 0.2 times the length of the walls. The boundary elements of the wall panels are explicitly presented in Fig. 1. The axial load acting on specimens HSCW1 and STHSW2 was 1400 kN, and the axial load ratio was 0.16, whereas the axial load acting on STHSW3 was 1700 kN, and the axial load ratio was 0.19. The experimental results proved that the specimens failed in the flexural mode.

2.2 Material properties

The concrete adopted in this study had a strength grade of C65, and the water-to-gel ratio was 0.28. The cement mixture adopted for HSC consisted of coarse aggregate: fine aggregate: fly ash: mineral powder: water reducer: water in a ratio of 1.0:2.5:1.53:0.11:0.2:0.02: 0.366. The
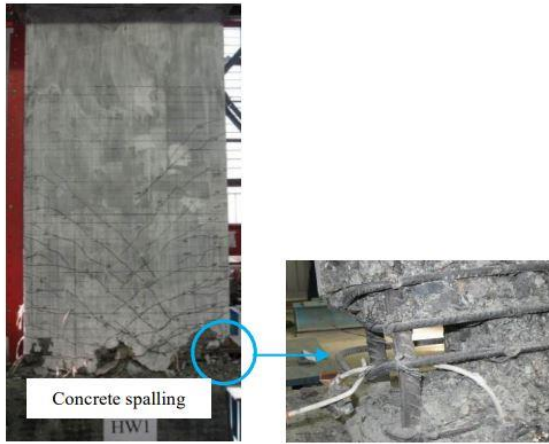
(a) Cracking and failure patterns

(b) Damage near wall ends

Fig. 4 Failure phenomenon of specimen HSCW1
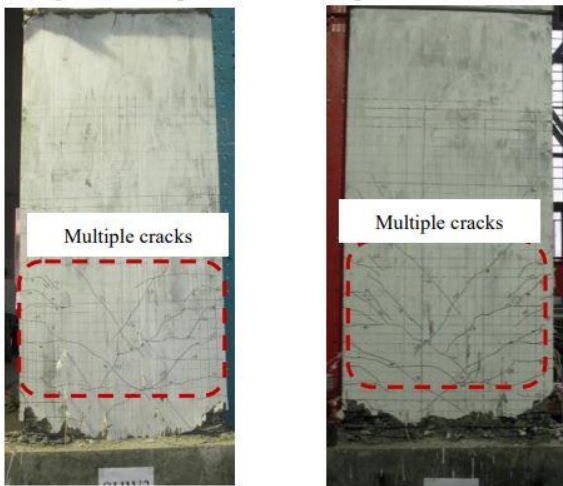
(a) Cracking and failure patterns of STHSW2

(b) Cracking and failure patterns of STHSW3
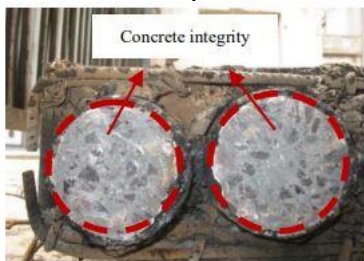
(c) Failure patterns of concrete confined by the steel tubes

Fig. 5 Failure phenomenon of specimen STHSW2 and STHSW3

actual compressive strength of the wall concrete was tested using cubes with sizes of 150 mm. The measured average compressive strengths for the cubic specimens were 71.9, 68.5, and 75.4 MPa. The steel tubes were fabricated using Grade Q345B steel. HRB400 was adopted for the D8 and D18 re-bars, and HPB300 was adopted for the A6.5 re-bar. The measured yield and ultimate strengths of the re-bars and steel tubes are summarized in Table 1.

(a) HSCW1

(b) STHSW2

(c) STHSW3
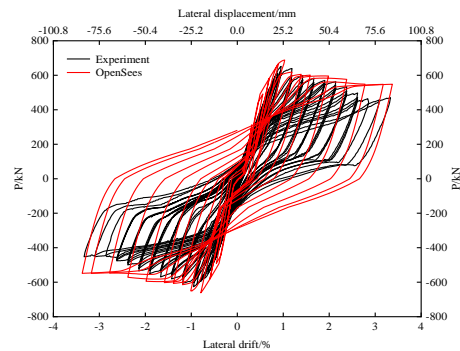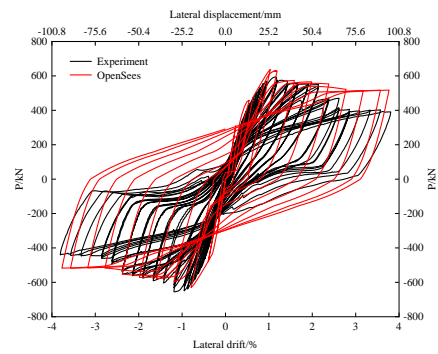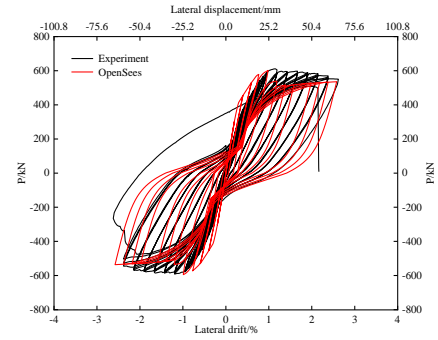
Fig. 6 Load-displacement hysteresis curves of specimens

2.3 Test set-up and procedure

The test set-up is illustrated in Fig. 2, including the tested specimens, loading frame, vertical jack used to apply a constant axial load, hydraulic actuator adopted to apply a cyclic lateral load, and reaction wall to support the actuator. A steel beam was placed on the top of the wall to distribute the axial force uniformly along the wall section, and the vertical jack was capable of moving horizontally to accommodate lateral deformation. An axial load was first imposed onto the specimens and maintained constant during the test. Thereafter, a cyclic lateral load was applied using the hydraulic actuator. Fig. 3 displays the detailed loading procedure followed during the tests. Before the specimens yielded, each level of the displacement cycle was loaded once, and the displacement loading amplitudes were incremented by 2 mm. After the specimen yielded,

(a) HSCW1

(b) STHSW2

(c) STHSW3
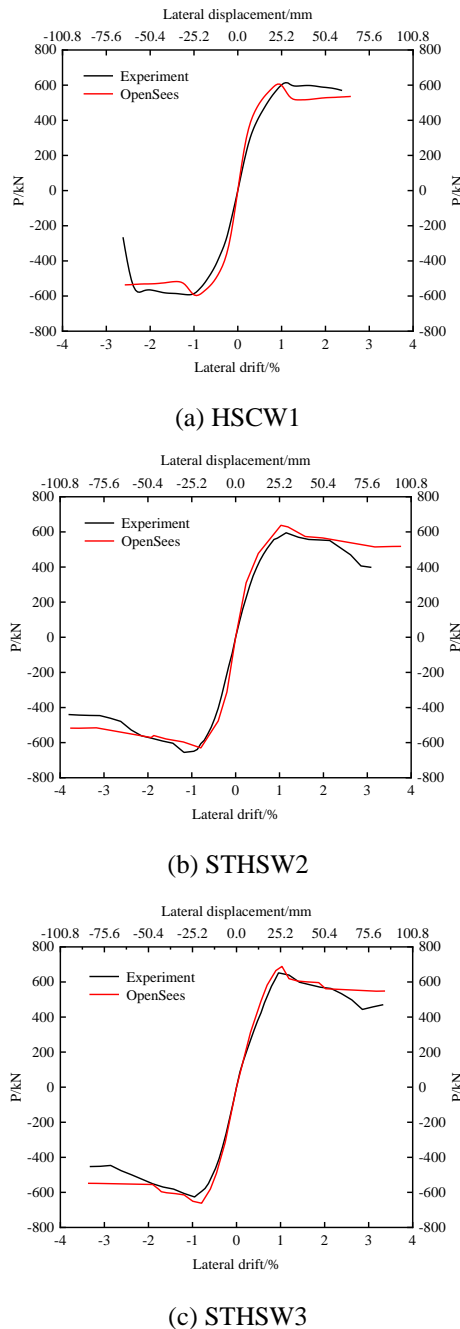
Fig. 7 Skeleton curves of specimens

multiples of 6 mm were imposed, and subsequent cycles were repeated three times. The test was terminated while the lateral load dropped to 85% of the peak load.

3. Experimental results and analysis

3.1 Failure pattern

Under a combined action of the constant axial load and cyclically increasing lateral load, the steel tubes and the longitudinal reinforcements at the boundary elements of the wall panels yielded, the concrete in the compressive regions

underwent severe cracking, and all the specimens experienced flexural failure. Figs. 4 and 5 illustrate the failure patterns for the tested specimens. For specimen HSCW1, with an ordinary stirrup-confined configuration, the concrete at the confined zone of the wall bottom was crushed and almost completely spalled (see Fig. 4). After application of the peak load, specimen HSCW1 completely lost its load-bearing capacity and underwent a sudden disintegration failure. As illustrated in Fig. 5, the failure patterns exhibited by specimens STHSW2 and STHSW3 are approximately similar. The first horizontal cracks occurred at the bottom of the tensile side. As the load increased, the steel tubes yielded.

With the increasing of load, the concrete outside the steel tubes exhibited spalling, thereby exposing the steel tubes.After the peak load, the load-bearing capacity of specimens STHSW2 and STHSW3 decreased slightly, and the specimens did not undergo disintegration owing to the presence of steel tubes. The final crack distributions and failure patterns of the aforementioned specimens are displayed in Figs. 5(a)-5(b). After the test, the steel tubes of specimens STHSW2 and STHSW3 were cut, and the concrete confined by the steel tubes at the bottom of the specimens was found to be essentially intact, as illustrated in Fig. 5(c).

3.2 Hysteresis responses

The hysteretic and skeleton curves of test specimens are presented in Figs. 6-7. Specimen HSCW1 lost its load-bearing capacity after the peak load was applied and underwent sudden failure. Specimen STHSW2 was designed with the same axial load ratio as HSCW1; but, the hysteresis curve of STHSW2 has a greater range than that of HSCW1.

Comparisons among the specimens revealed that specimen STHSW2 was able to endure more loading cycles, which indicated a desirable deformation ability after the peak load. While the axial force ratio of STHSW3 was higher than that of HSCW1, specimen STHSW3 still exhibited stable lateral resistance under a larger lateral drift. Thus, it is demonstrated that the brittle failure pattern demonstrated by HSC walls can be prevented by embedding steel tubes at the walls' boundary elements, and the hysteresis characteristics are also improved.

3.3 Bearing capacity and ductility

The measured loads and corresponding displacements of the specimens under characteristic conditions are listed in Table 2. The energy equivalent method (Park 1988) was adopted to determine the yield condition of the specimens; herein, the ultimate condition refers to the point when the load-bearing capacity decreases to 85% of the peak load. Correspondingly, the displacement ductility coefficient is calculated based on the ratio of the ultimate displacement to the yield displacement. According to Table 2, the cracking loads of the specimens increase with an increase in the axial compressive ratio. For the peak loads, the values of STHSW2 are greater than those of HSCW1 under the same

Table 2 Characteristic points of specimens

Specimens	Loading direction	P_{cr} /kN	P_y /kN	Δ_y /mm	P_m /kN	P_{FE} /kN	Δ_m /mm	P_u /kN	Δ_u /mm	θ_u	μ
HSCW1	(+)	373	478.2	12.3	611.0	601.9	24.8	550.0	48.1	1/52	3.9
	(-)	-	489.0	13.3	591.8	594.6	25.9	503.7	50.4	1/50	3.7
STHSW2	(+)	405	418.8	13.1	594.7	637.4	29.1	505.5	60.4	1/42	4.6
	(-)	-	506.9	13.8	655.6	630.4	29.5	557.2	64.6	1/39	4.7
STHSW3	(+)	462	424.4	14.0	651.8	688.4	24.1	554.0	56.3	1/45	4.0
	(-)	-	495.3	13.5	626.3	661.7	24.0	532.3	52.0	1/48	3.9

*Where, P_{cr} is cracking load, P_y, Δ_y is yield load and displacement, P_m, Δ_m is peak load and displacement, P_{FE} is the FEM values for peak load, P_u, Δ_u is ultimate load and displacement, μ is ductility coefficient.
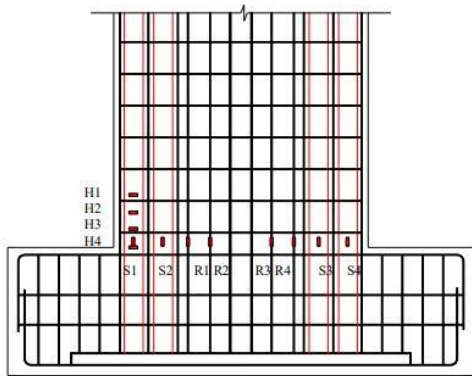
(a) distribution of strain gauges
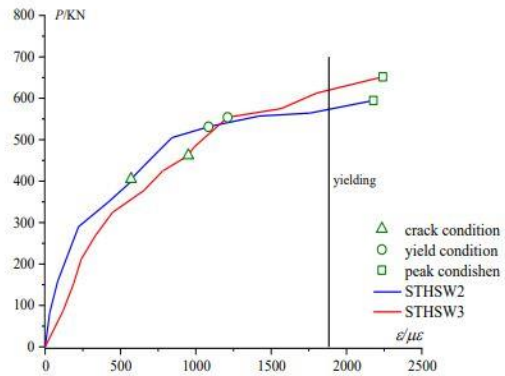
(b) longitudinal strain of S1 for STHSW2 and STHSW3 specimens
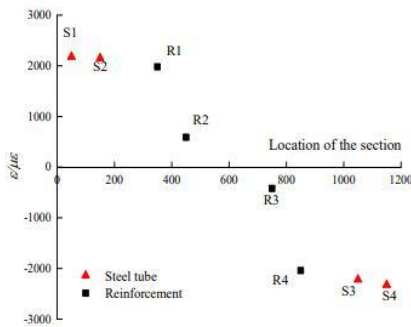
(c) longitudinal strain distribution of STHSW2 at peak load
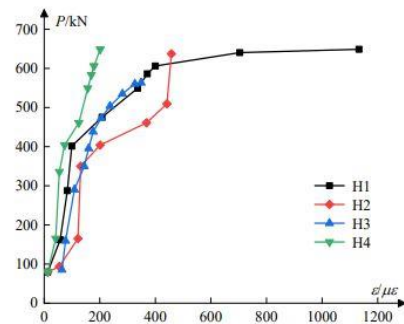
(d) hoop strain for steel tube of STHSW2

Fig. 8 Load-strain curves of specimens

axial compressive ratio. Compared to specimen STHSW2, the higher axial compressive ratio of STHSW3 results in a higher peak load. By comparing the ductility of each specimen, it can be ascertained that the deformation ability of STHC composite walls is improved compared with that of HSC walls. When the axial load ratio is constant, the displacement ductility of specimen STHSW2 increased by21% compared with that of specimen HSCW1. The axial load ratio of specimen STHSW3 was larger than that of specimen HSCW1; but, the displacement ductility of specimen STHSW3 was not lower than that of specimen HSCW1.

3.4 Strain analysis

The strain developments in the steel tubes and distributional vertical re-bars of specimens were measured during testing, and the locations of the strain gauges are presented in Fig. 8(a). Fig. 8(b) presents the longitudinal strain S1 acting at the bottom of the steel tubes, obtained from the STHC composite walls.

As can be seen, when the specimens reach cracking condition, the corresponding strain values were 570.70, and 950.25, respectively. The strains of steel tubes increase gradually with an increase in the horizontal load.When the peak loads were reached, the bottom section of the steel tubes yield. This indicates that the mechanical character of the steel tubes is sufficiently utilized in STHC composite walls. This indicates that the mechanical character of the steel tubes is sufficiently utilized in STHC composite walls. This indicates that the mechanical character of the steel tubes is sufficiently utilized in STHC composite walls. The
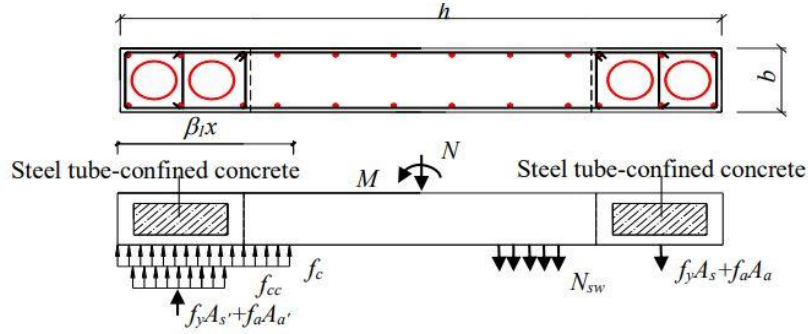
Fig. 9 The distribution of stress at peak bearing capacity

longitudinal strains of the steel tubes and distributional vertical re-bars at different locations along the bottom section are presented in Fig. 8(c) for specimen STHSW2. The measured strains indicate that the strain distribution approximately satisfies plane-section assumption when the specimen reaches the peak capacity.

The circumferential strains of the steel tubes in specimen STHSW2 were analyzed as typical circumferential strains for STHC composite walls. As presented in Fig. 8(d), the circumferential strains H1–H4 were measured at a spacing of 100 mm, where H1 is located at the bottom section of the steel tubes. The circumferential strains of the steel tubes gradually developed with the increasing horizontal load, which indicated that the confined stress resulting from the steel tubes applied to the core concrete increased as well. The circumferential strains at the bottom section of steel tubes, by contrast, were relatively higher than those at other locations. The aforementioned observations indicate that the confinement effect exerted by the steel tubes is more completely developed for the bottom section.

4. Bearing capacity prediction for STHC composite walls

4.1 Analytical model

According to the failure modes of STHC composite walls in this study, the test specimens exhibited a flexure-dominated failure, and the load-bearing capacity can be calculated by the flexural strength at the wall's bottom section. When calculating the load-bearing capacity of STHC composite walls, the following assumptions were employed: (1) The cross-section remained plane and bending, and the strain distributions along the cross-section conformed to the linear rule. (2) The concrete strength inside the steel tubes, calculated via the model suggested by Han *et al*. (2008, 2016), was assumed to be f_{cc}, considering the confinement effect of steel tubes. While the compressive strength of unconfined concrete was adopted for the concrete present outside the steel tubes, the stress was simply calculated by using the rectangular stress block model with two equivalent factors, α and β, which were assumed to be 0.97 and 0.77, respectively (GB50010 2010). (3) The tensile strength of the concrete was neglected. (4)

The contribution of distributional vertical re-bars, which were installed within a distance of $1.5x$ from the extreme compressive fiber, was ignored because such re-bars were close to the netural axis, and the stress was not completely utilized. Based on the above analysis, the section stress distribution diagram corresponding to the peak condition is stated in Fig. 9. The force equilibrium relationship is established.

$$N = N_c + N_{cc} + N_a + N_s - N_a^{'} - N_s^{'} - N_{sw} \tag{1}$$

$$N_{sw} = b f_{yw}(h_0 - 1.5\beta_1 x)\rho_{sw} \tag{2}$$

$$N_c = \alpha_1 f_{c} b \beta_1 x - f_c A_{cc} \tag{3}$$

$$N_{cc} = f_{cc} A_{cc} \tag{4}$$

where N denotes the axial load applied to the STHC composite walls, N_c and N_{cc} denote the compressive forces provided by the steel tube-confined concrete and unconfined concrete, respectively, N_{sw} denotes the tensile force provided by the distributional vertical rebars, f_{yw} and ρ_{sw} denote represent the yield strength and reinforcement ratio of the vertical distributional re-bars, respectively, x denotes the depth of the compression zone at the peak state, and h_0 and b denote the effective depth and thickness of the cross-section.

The stress–strain relationships of steel tubes and re-bars were idealized via an elastic–plastic approximation without considering strain hardening; therefore, the tensile and compressive forces acting on the steels in the boundary elements could be calculated as

$$\begin{cases} N_a = f_a A_a \\ N_a^{'} = f_a^{'} A_a^{'} \\ N_s = f_y A_s \\ N_s^{'} = f_y^{'} A_s^{'} \end{cases} \tag{5}$$

$$\begin{cases} N_a = N_a^{'} = f_a A_a \\ N_s = N_s^{'} = f_y A_s \end{cases} \tag{6}$$

The steel-tube-confined concrete strength f_{cc} can be calculated by Eqs. (7)-(8), which consider the increase in the concrete strength resulting from the confinement effect

of the steel tubes (Han *et al.* 2008, 2016).

$$f_{cc} = \left[1 + \left(-0.054\xi^2 + 0.4\xi \right) \left(\frac{24}{f_c} \right)^{0.45} \right] f_c \qquad (7)$$

$$\xi = \frac{f_a A_a}{f_c A_{cc}} \qquad (8)$$

where ξ represents the confinement coefficient to reflect the degree of confinement of the core concrete by the steel tubes, f_c represents the unconfined concrete strength, f_a and A_a represent the yield strength and cross-sectional areas of the steel tubes, respectively, and A_{cc} represents the cross-sectional area of core concrete in the steel tubes.

Therefore, the depth of the compression zone at the peak condition is as follows:

$$x = \frac{N - \left(f_{cc} - f_c \right) A_{cc} + b h_0 f_{yw} \rho_{sw}}{\beta_1 \left(\alpha_1 f_c + 1.5 f_{yw} \rho_{sw} \right)} \qquad (9)$$

According to the moment equilibrium with respect to the centroid of the boundary element in the tensioned region, the bending moment of the section center of the STHC composite walls can be calculated by Eq. (10).

$$\begin{aligned} M &= f_a' A_a' \left(h_0 - a' \right) + f_y' A_a' \left(h_0 - a' \right) \\ &+ N_c \left(h_0 - \beta_1 x / 2 \right) + N_{cc} \left(h_0 - 0.1h \right) \\ &- 0.5 N_{sw} \left(h_0 - 1.5\beta_1 x \right) \end{aligned} \qquad (10)$$

Consequently, the predicted load-carrying capacity P_c can be calculated, which includes the P-Δ effect (Park and Eom 2007):

$$P^c = \frac{M - N\Delta_p}{H} \qquad (11)$$

where H represents the height calculated from the lateral loading point to the wall base, and Δ_p represents the lateral displacement under the peak state.

4.2 Validation and comparison of the analytical model

In addition to the test results from specimens evaluated in this investigation, experimental data for other composite walls with steel tubes were selected from Qian *et al.* (2008, 2012), Cao *et al.* (2008a, 2008b, 2008c), Zhao *et al.* (2020), and Yang *et al.* (2014) to verify the accuracy of the analytical model.

In order to investigate the influence of steel tube confined effect on the bearing capacity of STHC composite walls, the analytical models with and without considering confinement effect of steel tubes were conducted and compared. Fig. 10 and Table 3 compare the experimental values with the theoretical results estimated by the analytical models in this study.

According to Table 3, the values of predicted peak bearing capacity P^{c1} are significantly lower than the experimental results. It is demonstrated that the load-bearing capacity of STHC composite walls was underestimated when the effect of steel tubes was not
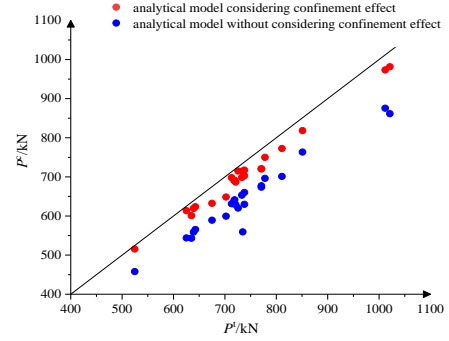
Fig. 10 Comparison of calculated results with experimental results

considered. In comparison, the test-to-calculated ratios of P^{c2}/P^t obtained from the proposed model considering the confinement effect of steel tubes range from 0.92 to 0.98 with a mean value of 0.96 and a variable coefficient of 0.017. The predicting results P^{c2} are in good agreement with the test values; this demonstrates the reliability and accuracy of the proposed analytical method considering the confinement effect of steel tubes in predicting the load-bearing capacity of STHC composite walls.

Moreover, as presented in Table 3, the compressive strength of concrete in those composite walls varied from 30.1 MPa to 101.7 MPa, and the analysis is in agreement with the experimental results. It demonstrates that this analytical model can be vindicated to both high-strength and normal-strength composite walls.

5. FEM analysis

Due to the limited number of specimens, only two axial load ratios were involved in the experimental study, i.e., 0.16 and 0.19. In order to investigate the influence of the high axial load ratio on the mechanical properties of STHC composite walls, different axial load ratios were adopted as 0.15, 0.20, 0.25, and 0.30. Moreover, certain other factors such as the strength of the steel tubes and the shear-span ratio are also known to affect the mechanical properties of STHC composite walls. However, before evaluating the effect produced by other parameters, a valid FEM should be established according to the current experiments; thereafter, on successful validation of the accuracy of the proposed method via comparisons between the experimental results and simulation outputs, an FEM with different parameters can be utilized for further investigations on the mechanical properties of STHC composite walls.

To further evaluate the effect of various parameters on the performance of STHC composite walls, an FEM was established by using the numerical package OpenSees.

5.1 Element types

The multi-layer shell element and fiber beam-column element were used to establish an FEM of the STHC composite walls considered in this study, as presented in Fig. 11.

Table 3 Comparison of the measured and calculated results

Reference	Specimens	f_{c1} / Mpa	f_{c2} / Mpa	Experimental value P^t / KN	Calculation value P^{c1} / KN	P^{c2} / KN	P^{c1} / P^t	P^{c2} / P^t
This study	STHSW2	71.9	71.9	625.2	543.8	613.6	0.87	0.98
	STHSW3	71.9	71.9	639.1	558.9	619.4	0.87	0.97
Qian et al. (2008)	CIW-H2	42.3	42.3	524.5	457.8	515.6	0.87	0.98
	SW2	57.5	44.3	718.0	639.0	690.4	0.89	0.96
	SW3	57.5	40.5	738.0	629.9	702.9	0.85	0.95
Qian et al. (2012)	SW4	57.5	40.1	771.0	673.6	720.6	0.87	0.93
	SW5	57.5	46.7	719.0	641.3	691.3	0.89	0.96
	SW6	57.5	49.8	851.0	763.4	818.2	0.90	0.96
	SW7	57.5	47.3	721.0	628.6	686.7	0.87	0.95
Cao et al. (2008)	SW2	60.1	60.1	734.7	559.3	714.9	0.76	0.97
	SW3	60.1	60.1	725.7	620.2	714.9	0.85	0.99
Cao et al. (2008)	SW2	30.1	30.1	642.6	565.5	623.7	0.88	0.97
Cao et al. (2008)	SW4	60.1	60.1	635.0	543.1	601.0	0.86	0.95
	S01	101.7	66.9	811.0	701.2	772.5	0.86	0.95
	S02	92.6	66.9	778.0	696.3	749.9	0.89	0.96
	S04	92.6	57.1	733.0	653.2	698.6	0.89	0.95
	S05	92.6	57.1	771.0	677.1	720.4	0.88	0.93
Fang et al. (2013)	S06	92.6	57.1	702.2	599.6	648.5	0.85	0.92
	S07	92.6	57.1	713.0	631.3	698.0	0.89	0.98
	S09	92.6	57.1	738.0	660.2	717.3	0.89	0.97
	S10	92.6	57.1	675.0	589.3	632.4	0.87	0.94
Yang et al. (2014)	SW6	57.1	57.1	1012.0	875.5	973.3	0.87	0.96
	SW8	57.1	57.1	1021.0	861.4	981.6	0.84	0.96
Mean value	—	—	—	—	—	—	0.87	0.96
variable coefficient	—	—	—	—	—	—	0.028	0.017

*Where f_{c1} and f_{c2} are the compressive strength of concrete inside and outside of the steel tube, respectively, P^{c1} and P^{c2} are the calculation value without and with considering confinement effect of steel tubes.
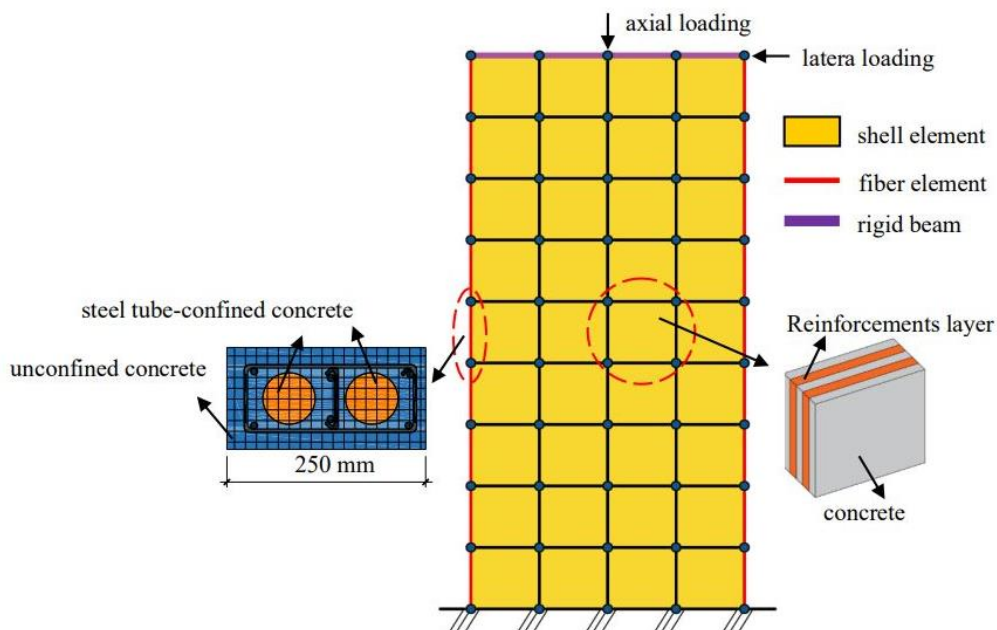
Fig. 11 Finite element mesh and boundary conditions

The multi-layer shell element was used to simulate the wall web. The web section was divided into a number of concrete and reinforcement layers along the depth. Additionally, the boundary elements of the wall panels were modeled using the fiber beam-column element, and the fiber beam-column element and multi-layer shell element shared the same nodes at the boundary region. The section of boundary elements was classified into the following two categories to account for the confining effect: steel tube-confined concrete and unconfined concrete.

5.2 Constitutive laws of materials

5.2.1 Constitutive relationships of concrete

The material model Concrete02 (Mazzoni *et al.* 2006) in the OpenSees program was utilized to model the properties of concrete in the STHC composite walls. For steel tube-confined concrete, the compressive stress and corresponding strain were computed based on the equation proposed by Han *et al.* (2008, 2016), which is described as follows:

$$y = \begin{cases} 2\left(\dfrac{\varepsilon}{\varepsilon_{cc}}\right) - \left(\dfrac{\varepsilon}{\varepsilon_{cc}}\right)^2 & \varepsilon \le \varepsilon_{cc} \\[2em] \dfrac{\dfrac{\varepsilon}{\varepsilon_{cc}}}{\beta\left(\dfrac{\varepsilon}{\varepsilon_{cc}} - 1\right)^2 + \dfrac{\varepsilon}{\varepsilon_{cc}}} & \varepsilon > \varepsilon_{cc} \end{cases} \tag{12}$$

Where $\varepsilon_{cc} = \varepsilon_c + \left[1400 + 800\left(\frac{f_c}{24} - 1\right)\right]\xi^{0.2}(\mu\varepsilon)$, ε_{cc} denotes the peak compressive strain of steel tube-confined concrete, ε_c denotes the peak compressive strain of unconfined concrete, $\varepsilon_c = 1300 + 12.5f_c (\mu\varepsilon)$, β denotes a coefficient, and $\beta = (2.36 \times 10^{-5})^{[0.25+(\xi-0.5)^7]}f_c^2 \times 3.51 \times 10^{-4}$

The compression constitutive relation proposed in the GB50010 (2010) was adopted to evaluate the unconfined concrete present in STHC composite walls. The stress–strain relationship can be modeled as in Eqs. (13)-(14):

$$y = \begin{cases} \dfrac{nx}{n-1+x^n} & (x \le 1) \\[1.5em] \dfrac{x}{\alpha_c(x-1)^2 + x} & (x > 1) \end{cases} \tag{13}$$

$$n = \frac{E_c\varepsilon_0}{E_c\varepsilon_0 - \sigma_0} \tag{14}$$

Where α_c denotes a parameter introduced for controlling the shape of the curve, and E_c denotes theelastic modulus of unconfined concrete.

5.2.2 Constitutive relationships of structural steels

For the steel tubes and re-bars in the FEM, the Steel02 (Mazzoni *et al.* 2006) model in the OpenSees program was used to model the mechanical properties of structural steels. The shapes of the loading and unloading curves under cyclic loading can be controlled via parameters sR0, cR1,
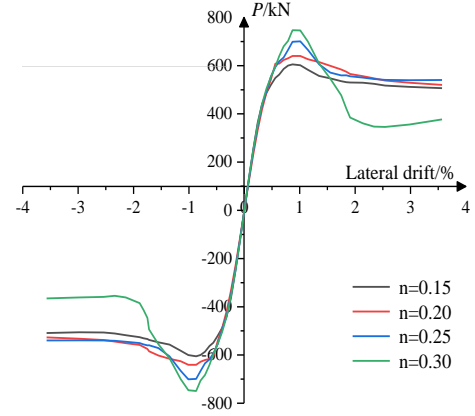
(a) skeleton curves
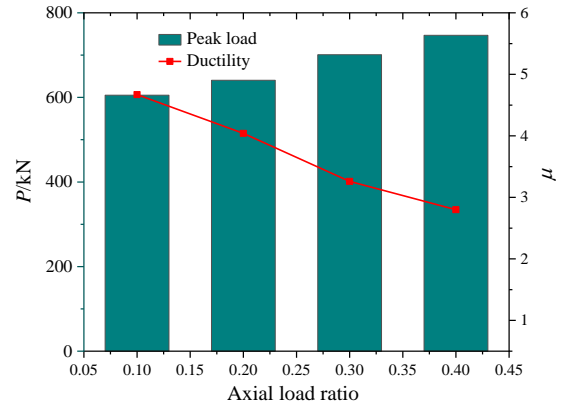
(b) peak load and ductility

Fig. 12 Influence of axial load ratio

and cR2. R0 denotes the initial curvature between the elastic and post-yield slopes, while cR1 and cR2 denote the curvature variation parameters of the Bauschinger curve after each strain reversal. The parameters R0, cR1, and cR2 were assumed to be 18.5, 0.925, and 0.15 for steel, in accordance with the recommendations provided by Taucer *et al.* (1991).

5.3 Boundary conditions and loading

Fig. 11 illustrates the element mesh and boundary conditions of the FEM. The displacements and rotations of the nodes at the base of the FEM were completely constrained. A rigid beam was placed on the top of the wall to simulate the loading beam to prevent crushing of the local concrete when subjected to an axial load. Following the application of an axial pressure, a cyclic displacement loading was imposed to the rigid beam in accordance with the testing procedures.

5.4 Verification of the FEM

According to aforementioned modeling approach, various FEMs of the STHC composite walls were established. The hysteresis and skeleton curves obtained from the FEMs and tests are illustrated in Figs. 6-7, respectively. As displayed in the comparison results, the proposed FEM can provide quite accurate predictions for

Table 4 Influence of axial load ratio on bearing capacity and ductility

n	P_y / kN	Δ_y / mm	θ_y	P_m / kN	Δ_m / mm	θ_m	P_u / kN	Δ_u / mm	θ_u	μ
0.15	458.15	13.12	1/192	625.37	29.1	1/87	514.38	61.29	1/41	4.67
0.20	462.40	14.08	1/179	650.47	24.1	1/105	544.98	56.98	1/44	3.94
0.25	525.71	15.84	1/151	700.84	23.2	1/109	595.39	51.68	1/49	3.26
0.30	576.80	17.08	1/139	746.96	22.8	1/113	634.17	47.84	1/53	2.80
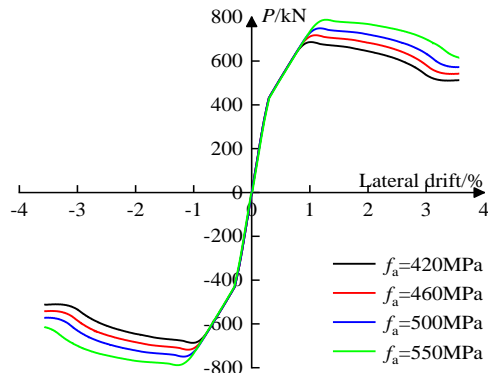
(a) skeleton curves
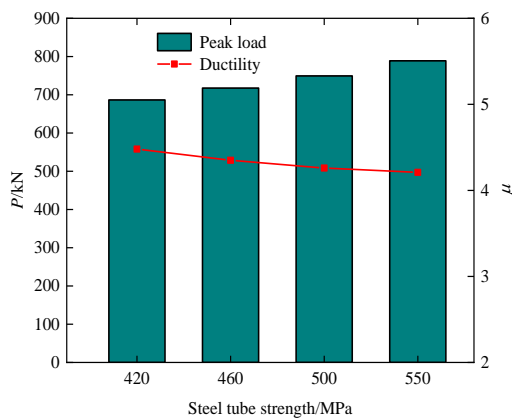
(b) peak load and ductility

Fig. 13 Influence of steel tube strengths

the hysteretic behavior. However, owing to ideal material and loading conditions, initial defects in the wall panels were not entirely considered in the FEM, resulting in the initial stiffness obtained from the FEM being slightly larger than the experimental values.

Table 2 compares the peak bearing capacity obtained from the FEM and experiment. As can be observed, the FEM can accurately predict the peak strength with an average error of 4.0%. Therefore, the FEM developed in this investigation can accurately simulate the mechanical properties of SHTC composite walls, indicating that the FEM is reasonable.

5.5 Parameter analysis

Based on the FEM validated by the experimental results, a parametric analysis was systematically conducted to investigate the influences of various parameters on the

mechanical properties of the STHC composite walls. The FEM corresponding to STHSW2 was selected as the benchmark model in the analysis.

5.5.1 Axial load ratio

The skeleton curves of the STHC composite walls with different axial load ratios are presented in Fig. 12(a).

In comparison, the higher the axial load ratio, the greater the increase in the peak bearing capacity of the STHC composite walls. As the axial load increase, the skeleton curves of the STHC composite walls present a more evident declining stage after the peak load. As illustrated in Table 4, when the axial load ratio increases from 0.15 to 0.3, the peak load increases from 605.37KN to 746.96KN, but the ductility coefficient decreases from 4.67 to 2.80. Therefore, the load-bearing capacity can be improved with an increase in the axial load ratio; but, the ductility of the STHC composite wall is found to decrease.

5.5.2 Steel tube strength

The strength of steel tubes was set to four different levels: 420, 460, 500, and 550 MPa. The skeleton curves of the STHC composite walls with different steel tube strengths are presented in Fig. 13(a), which were obtained from the hysteretic curves. The steel tube strength essentially exhibits no influence on the initial stiffness of the STHC composite walls, and the aforementioned skeleton curves coincide with each other at the initial loading stage. In comparison, the higher the strength of the steel tubes, the greater the increase in the peak bearing capacity of the STHC composite walls. Beyond the peak load, the degradation rate of the load-bearing capacity of STHC composite walls with different steel tube strengths demonstrates no significant difference. The peak load and ductility coefficient of the aforementioned models are presented in Fig. 13(b) and Table 5. When the steel tube strength increases from 420 to 550 MPa, the peak bearing capacity improves by 14.90%, while the ductility coefficient of the STHC composite walls decreases by 6.03%. Thus, the ultimate and yield drifts improve with the increase in the steel tube strength, while the increase in the ultimate drift is less than that in the yield drift. Consequently, the ductility coefficient of the STHW composite walls slightly decreases.

5.5.3 Shear-span ratio

To analyze the effect of the shear-span ratio on the mechanical properties of the STHC composite walls, different shear-span ratios were adopted as 2, 3, 4 and 5. The skeleton curves of the STHC composite walls obtained from the FEM results are presented in Fig. 14. It can be

Table 5 Influence of steel tube strengths on bearing capacity and ductility

f_a / MPa	P_y / kN	Δ_y / mm	θ_y	P_m / kN	Δ_m / mm	θ_m	P_u / kN	Δ_u / mm	θ_u	μ
420	569.92	15.30	1/165	686.47	25.6	1/98	583.50	68.63	1/37	4.48
460	589.90	16.47	1/153	717.64	27.6	1/91	609.99	71.61	1/35	4.35
500	610.48	17.65	1/143	749.33	29.6	1/85	636.93	75.22	1/33	4.26
550	636.50	19.15	1/132	788.73	32.0	1/79	670.17	80.68	1/31	4.21

Table 6 Influence of shear-span ratio on bearing capacity and ductility

λ	P_y / kN	Δ_y / mm	θ_y	P_m / kN	Δ_m / mm	θ_m	P_u / kN	Δ_u / mm	θ_u	μ
2	537.07	14.32	1/168	635.72	23.8	1/101	540.36	62.94	1/38	4.40
3	389.16	18.26	1/197	420.10	28.2	1/128	357.08	90.67	1/40	4.97
4	284.34	25.71	1/187	315.90	44.0	1/109	268.52	156.09	1/31	6.07
5	223.06	32.13	1/186	249.33	64.8	1/93	211.93	207.25	1/28	6.45

(a) skeleton curves

(b) peak load and ductility
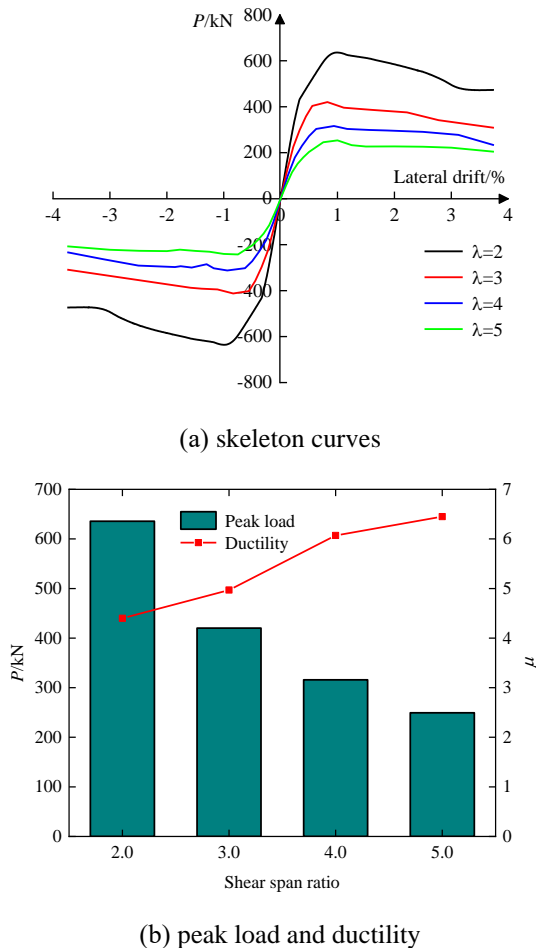
Fig. 14 Influence of shear-span ratio

seen that the initial stiffness and bearing capacity decrease with an increase in the shear-span ratio. As the shear-span ratio increases, the bearing capacity of the STHC composite walls decreases more gradually after the peak load, and the deformation capacity of the STHC composite walls also improves.

Table 6 indicates that the peak load decreases by 60.78% when the shear-span ratio increases from 2 to 5.

The ductility coefficient of the STHC composite wall is 4.40 when the shear-span ratio is 2, and the coefficient reaches 6.45 when the shear-span ratio is 5.

6. Conclusions

The mechanical behavior of STHC composite walls under a constant axial load and cyclically increasing lateral load was investigated. The conclusions were drawn from the experimental observations, theoretical analysis, and FEM simulations.

(1) By confining the wall panels using steel tubes, the load-bearing capacity and ductility of the tested specimens improved. The STHC composite walls withstood more loading cycles and exhibited more stable hysteresis property than the ordinary HSC walls. After the peak load, the load-bearing capacity of the STHC composite walls decreased gradually, and the walls did not undergo disintegration owing to the action of steel tubes.

(2) An analytical model, which accounted for the confinement effect provided by steel tubes, was proposed to analyze the flexural load-bearing capacity of the STHC composite walls. The results provided by this model demonstrated good agreement with the test results, indicating that the proposed model could be adopted to predict the loading-bearing capacity of STHC composite walls.

(3) An FEM for STHC composite walls was established based on reasonable constitutive models for materials and the confinement effect provided by the steel tubes. The FEM results agreed well with the experimental results in the aspect of the hysteretic curves, load-deflection curves, and peak loads.

(4) Based on the experimental and FEM results, a parameter analysis was conducted to investigate the effects of various parameters on the mechanical properties of STHC composite walls, including the axial load ratio, shear-span ratio, and steel tube strength. The bearing capacity of the STHC composite walls increased with the increase of axial load ratio, but its ductility decreased. The load-bearing capacity could be improved with an increase in

the steel tube strength; but, the ductility of the STHC composite wall was found to decrease slightly. With the shear-span ratio increased, the bearing capacity of the STHC composite walls decreased significantly, whereas its deformation capacity improved.

Acknowledgments

References

Bai, L., Zhang, C. and Xiong, E. (2019), "Investigations on the shear mechanism of steel tube rein forced concrete shear walls with a low shear span ratio", *KSCE J. Civ. Eng.*, **23**(7), 2983-2996. https://doi.org/10.1007/s12205-019-1170-3.

Ćurković, I., Skejić, D., Džeba, I. and De Matteis, G. (2019), "Seismic performance of composite plate shear walls with variable column flexural stiffness", *Steel Comp. Struct.*, **33**(1), 851-868. https://doi.org/10.12989/ scs.2019.33.1.019.

Wan-Lin, C., Min, W. and Shao-He, W. (2008), "A seismic research of composite shear wall and core walls with rectangular concrete filled steel tube columns", *Eng. Struct.*, **25**, 58-70.

Cao, W., Wang, M. and Wang, S. (2008), "Seismic behavior research on composite shear wall with concrete filled steel tube columns in high axial-load ratio", *Earthq Eng Eng Vib.*, **28**(1), 85-90. https://doi.org/ 10.13197/j.eeev.2008.02.015.

Cao, W., Wang, M., Zhang J., Wang, S. and Zeng, B. (2008), "Seismic experiment and load-carrying capacity calculation of shear wall with concrete filled steel tube columns", *J B Univ Technol.*, **34**(12), 1291-1297. (in Chinese)

Dang, L., Pang, R., Liu, Y., Wang, Y., Wang, L. and Yang J. (2022), "Research on seismic performance of precast steel-concrete composite tube shear walls with horizontal joint", *Eng. Struct.*, **250**, https://doi.org/10.1016/ j. engstruct.2021.113409.

Fang, X., Li, Q., Wei, H., Zhou, Y., Jiang, Y. and Lai, H. (2013), "Experimental study on axial-flexural behavior of shear walls with steel tube-confined high performance concrete", *J. Build. Eng.*, **34**(8), 72-81. https://doi.org/10.14006/j.jzjgxb.2018.11.010.(in Chinese)

GB 50010 (2010), *Code for Design of Concrete Structures*, China Ministry of Construction: Beijing; China.

Gao, D., You, P., Zhang, L. and Yan H. (2018), "Seismic behavior of SFRC shear wall with CFST columns", *Steel Comp. Struct.*, **28**(5), 527-539. https://doi.org/10.12989/scs.2018.28.5.527.

Huang, F., Yu, X. and Chen, B. (2012), "The structural performance of axially loaded CFST columns under various loading conditions", *Steel Comp. Struct.*, **13**(5), 451-471. https://doi.org/10.12989 /scs. 2012.13.5.451.

Hou, H., Fu, W., Qiu, C., Cheng, J., Qu, Z., Zhu, W. and Ma, T. (2019), "Effect of axial compression ratio on concrete-filled steel tube composite shear wall", *Adv. Struct.*, **22**(3), 656-669. https://doi.org /10.1177/1369433218796407.

Han, L H., Tao, Z. and Yao, G.H. (2008), "Behaviour of concrete-filled steel tubular members subjected to shear and constant axial compression", *Thin Wall. Struct.*, **46**(7), 765-780. https://doi.org/10.1016/j.tws.2008.01.026.

Han, L. (2016), "Concrete filled steel tubular structures theory and practice", *Beijing: Science Press*, China.

Ji, X., Sun, Y., Qian, J. and Lu, X. (2015), "Seismic behavior and modeling of steel reinforced concrete (SRC) walls", *Earthq. Eng. Struct. D.*, **44**, 955-72. https://doi.org/10.1002/eqe.2614.

Li, X., Zhang, J. and Cao, W. (2020), "Hysteretic behavior of high-strength concrete shear walls with high-strength steel bars: Experimental study and modelling", *Eng. Struct.*, **214**, https://doi.org/10.1016/j.engstruct.2020.110600.

Liang, W., Dong, J. and Wang, Q. (2018), "Axial compressive behavior of concrete-filled steel tube columns with stiffeners", *Steel Comp. Struct.*, **29**(2), 151-159. https://doi.org/10.12989/scs.2018.29.2.151.

Liao, F.Y., Han, L.H. and Tao, Z. (2009), "Seismic behaviour of circular CFST columns and RC shear wall mixed structures: experiment", *J. Constr. Steel Res.*, **65**(8-9), 1582-96. https://doi.org/10.1016/j.jcsr.2009.04.023.

Mazzoni, S., McKenna, F., Scott, M.H. and Fenves, G.L. (2006), *OpenSees Command Language Manual*, Pacific Earthquake Engineering Research (PEER) Center.

Paulay, T. and Priestley, M.J.N. (1992), "Seismic design of reinforced concrete and masonry buildings", *Wiley Interdiscip. Rev. Water.*, **30**(04), https://doi.org/10.1002/ 9780470172841.

Park, H. and Eom, T. (2007), "Truss model for nonlinear analysis of RC members subject to cyclic loading", *J. Struct. Eng.* **133**(10), 1351-63. https://doi.org/10.1061/(ASCE)0733-9445(2007)133:10(1351).

Park, R. (1988), "State of the art report ductility evaluation from laboratory and analytical testing", *Proceedings of Ninth World Conference on Earthquake Engineering*, Tokyo, Kyoto, Japan, 605-616.

Qian, J., Wei, Y., Zhang, Z., Cai, Y., Yu, Y. and Shen, L. (2008), "Experimental study on seismic behavior of SRC shear walls with high axial force ratio", *J. Build. Eng.*, **29**(4), 43-50. https://doi.org/10.14006/ j.jzjgxb.2008.02.008.

Qian, J., Jiang, Z. and Ji, X. (2012), "Behavior of steel tube-reinforced concrete composite walls subjected to high axial force and cyclic loading", *Eng. Struct.*, **36**, 173-84. https://doi.org/10.1016/j.engstruct.2011.10.026.

Qin, Y., Chen, X., Xi, W., Zhu, X. and Chen, Y. (2020), "Behavior of L-shaped double-skin composite walls under compression and biaxial bending", *Steel Comp. Struct.*, **37**(4), 405-418. https://doi.org/10.12989/scs.2020.37.4.405.

Teng, S. and Chandra, J. (2016), "Cyclic shear behavior of high-strength concrete structural walls", *ACI Struct. J.*, **113**(6), 1335-1345. https://doi.org/10.14359 /51689158.

Tong, X., Hajjar, J.F., Schultz, A.E. and Shield, C.K. (2005), "Cyclic behavior of steel frame structures with composite reinforced concrete infill walls and partially restrained connections", *J. Constr. Steel Res.*, **61**, 531-52. https://doi.org/10.1016/j.jcsr.2004.10.002.

Taucer, F., Spacone, E. and Filippou, F.C. (1991), *A Fiber Beam-Column Element for Seismic Response Analysis of Reinforced Concrete Structures*, Report UCB/EERC-91/17, Earthquake Engineering Research Center, University of California at Berkeley.

Xu, G., Wang, Z., Wu, B., Bursi, O.S., Tan, X., Yang, Q. and Wen, L. (2017), "Seismic performance of precast shear wall with sleeves connection based on experimental and numerical studies", *Eng. Struct.*, **150,** 346-58. https://doi.org/10.1016/j.engstruct.2017.06.026.

Guang, Y., Zhao, Zuozhou, Q.J. and Xu, L. (2014), "Experimental study on seismic behavior of a new type of concrete filled steel tube composite shear walls", *Bldg.*, **44**(7), 93-98. https://doi.org/10.19701/j.jzjg.2014.07.018.(in Chinese)

Younas, S., Li, D., Hamed, E. and Uy, B. (2021), "Behaviour of high strength concrete-filled short steel tubes under sustained loading", *Steel Comp. Struct.*, **39**(2), 159-170. https://doi.org/10.12989/scs.2021.39.2.159.

Zhou, J., Fang, X. and Yao, Z. (2018), "Mechanical behavior of a steel tube-confined high-strength concrete shear wall under combined tensile and shear loading", *Eng. Struct.*, **171**, 673-85. https://doi.org/10.1016 /j.engstruct.2018.06.024.

Zhao, N., Wang, Y., Han, Q. and Su, H. (2020), "Bearing capacity of composite shear wall incorporating a concrete-filled steel tube boundary and column-type reinforced wall", *Adv. Struct.*, **23**(10), 2188-2203. https:// doi.org/10.1177/1369433220911156.

Zhang, J., Li, X., Yu, C. and Cao, W. (2021), "Cyclic behavior of high-strength concrete shear walls with high-strength reinforcements and boundary CFST columns", *J. Constr. Steel Res.*, **182**(4), https://doi.org /10.1016/j.jcsr.2021.106692.

BU